ACS APPLIED MATERIALS & INTERFACES

Research Article

www.acsami.org

Ionic Liquid Integrated Multiwalled Carbon Nanotube in a Poly(vinylidene fluoride) Matrix: Formation of a Piezoelectric β-Polymorph with Significant Reinforcement and Conductivity Improvement

Amit Mandal and Arun K. Nandi*

Polymer Science Unit, Indian Association for the Cultivation of Science, Jadavpur, Kolkata 700 032, India

Supporting Information

ABSTRACT: Multiwalled carbon nanotubes (MWNTs) are functionalized covalently with ionic liquid (IL, 3-aminoethyl imidazolium bromide) which helps good dispersion of IL-functionalized MWNTs (MWNT-IL) in the poly(vinylidene fluoride) (PVDF) matrix. Analysis of transmission electron microscopy (TEM) micrographs suggests ~10 nm coating thickness of MWNTs by ILs, and the covalent linkage of ILs with MWNTs is confirmed from FT-IR and Raman spectra. PVDF nanocomposites with full β-polymorphic (piezoelectric) form are prepared using MWNT-IL by both the solvent cast and melt-blending methods. The FE-SEM and TEM micrographs indicate that IL-bound MWNTs are homogeneously dispersed within the PVDF matrix. Increasing MWNT-IL concentration in the composites results in increased β polymorph formation with a concomitant decrease of the α polymorph, and a 100% β polymorph formation occurs for 1 wt % MWNT-IL in both the fabrication conditions. A differential scanning calorimetry (DSC) study shows that the MWNT-ILs are an efficient nucleating agent for PVDF crystallization preferentially nucleating the β form due to its dipolar interactions with PVDF. The glass transition temperature (T_g) gradually increases with an increase in MWNT-IL concentration, and the storage modulus (G') of the composites increases significantly, showing a maximum increase of 101.3% for 0.5 wt % MWNT-IL. The Young's modulus increases with MWNT-IL concentration, and analysis of the data using the Halpin−Tsai equation suggests that at low concentration they adopt an orientation parallel to the film surface; however, at higher MWNT-IL concentration it is randomly oriented. The tensile strength also increases with an increase in MWNT-IL concentration, and both the Young's modulus and the tensile strength of solvent cast films are lower than melt-blended samples. The elongation at break in the solvent cast samples shows a maximum, but in melt-blended samples it decreases continuously with increasing MWNT-IL concentration. The composites exhibit a very low conductivity percolation threshold at 0.05 wt %, and the three-dimensional conducting network is produced. Higher conductivity (~1 S/cm for 1% MWNT-IL) than other MWNT/PVDF composites has been attributed to the anchored ionic liquid.

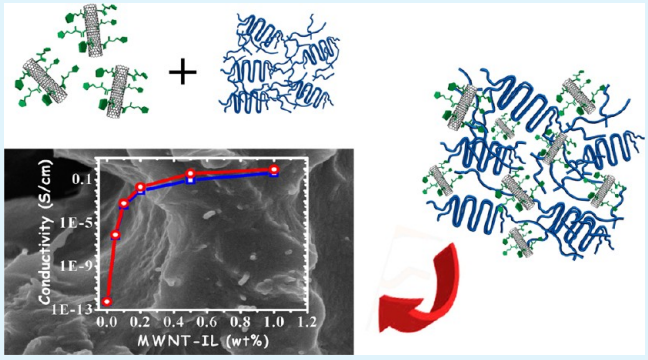

KEYWORDS: *homogeneous dispersion, Raman spectra, glass transition temperature, storage modulus, Halpin−Tsai equation, percolation threshold*

1. INTRODUCTION

Polymer nanocomposites have drawn considerable research interest because of their dramatic improvement in physical, thermal, mechanical, and electroactive properties compared to the pristine polymer.[1] Carbon nanotubes (CNTs) are ideal nanofillers for fabrication of multifunctional materials,[2−10] for it is superior electrical,[6] thermal,[7,8] and mechanical properties.[9] The electrical conductivity of an insulating polymer containing carbon nanotubes has drawn great research interest because of its potential applications in electrostatic dissipation[11,12] and in electromagnetic interference (EMI) shielding material.[13,14] However, the lack of good dispersion of CNTs in the polymer matrix due to its strong cohesive interactions complicates their use. Although several methods have been used to improve the compatibility between carbon nanotubes and the polymer matrix, the problem of homogeneous dispersion of CNTs in polymer matrices still persists for industrial applications.[15−17] The dispersion of CNTs in the polymer matrix has been improved with the help of surfactants or polymers[18−22] or by chemical modification.[23−27] In the chemical modification approach, the electrical and mechanical properties of the composites are comparatively less due to the loss of sp^2 structure and shortening of the length of CNTs, respectively.[28,29] The noncovalent wrapping of polymer or surfactant

Received: October 9, 2012
Accepted: December 30, 2012
Published: January 2, 2013

 © 2013 American Chemical Society

significantly improves nanotube dispersion within the polymer matrix, increasing the mechanical and conducting properties.[20−22,30] However, covalent integration of CNTs with the ionic moiety might improve the mechanical and conducting properties due to strong interfacial interaction and easier transport of charges.

Studies on piezoelectric and pyroelectric electroactive polymers have gained considerable attention in recent years because a host of novel applications can be envisaged for these materials due to their wide dynamic range of actuation, higher dielectric strength, and ferro-electric properties.[31−33]Among all the electroactive polymers, poly(vinylidene fluoride) (PVDF) and its copolymer are extensively studied by several research groups because of their largest piezoelectric and pyroelectric coefficient.[33] It is a technologically important engineering plastic in the chemical industry due to its remarkable weather and chemical resistance widening its applications in different fields.[33−36] There are five crystalline polymorphs of PVDF (α, β, γ, δ, and ε),[37] and among these the α polymorph is the most common produced in the melt crystallization, having a monoclinic unit cell with $TGT\overline{G}$ chain conformation.[38,39] The γ phase having an orthorhombic unit cell with a $T_3GT_3\overline{G}$ chain conformation is produced only from crystallization at high temperature and pressure.[40,41] The δ and ε polymorphs are polar and antipolar analogs of α and γ form, respectively.[42] The β-polymorph has an orthorhombic unit cell with all trans conformation and exhibits the highest piezoelectric, pyroelectric, and ferroelectric properties. Thus, the β polymorph of PVDF has drawn large attention from many researchers toward its formation and its technological utilization.[37,43]

A variety of experimental techniques have been developed to induce β phase formation, e.g., crystallization from solution,[41] melt crystallization at high pressure, application of a strong electric field,[44,45] mechanical deformation, etc.[46,47] Presently, nanofillers are in focus for enhancing the β polymorph formation in PVDF and stabilization which are achieved most recently by preparing composites with organically modified nanoclay,[41,48,49] metal nanoparticles,[50] functionalized multiwalled carbon nanotubes (MWNTs),[51,52] and graphene sheets.[53] Generally, in the preparation of PVDF/clay, PVDF/Ag, and PVDF/MWNT nanocomposites, the piezoelectric β polymorph PVDF is produced when made from the solution casting method, but in the melt quenching method, this β polymorph is not always retained. In the melt-cooled samples of PVDF/ester functionalized MWNT (5%) composites, a maximum of 50% β polymorph PVDF was achieved.[51] However, in the case of PVDF/unfunctionalized MWNT composites, only α polymorphic PVDF is produced in the melt-cooled condition.

Recently, ionic liquids (ILs) have been found to have strong interactions with polymers providing new possibilities to disperse carbon nanotubes in the polymer matrix, and few studies have succeeded in dispersing IL-modified CNTs through noncovalent interactions in polyurethane and PVDF matrices.[54a,b] In the present study, we have functionalized the multiwalled carbon nanotubes (MWNTs) with a widely used room-temperature ionic liquid, 3-aminoethyl imidazolium bromide. The MWNT-IL is then incorporated into the PVDF matrix by the solution blending and melt blending methods to fabricate the PVDF/MWNT-IL nanocomposites rendering the MWNT-IL to remain homogeneously dispersed in the PVDF matrix. In the noncovalent functionalization, Xing et. al have reported a mixture of β and γ polymorph formation at 2% (w/w) ionic liquid and MWNT contents.[54b] In the present study, the PVDF nanocomposite with 1% (w/w) of modified MWNT-IL has produced the 100% piezoelectric β-polymorph of PVDF at both the solvent-casting and melt-blended conditions. To our knowledge, this is the first report to achieve 100% β-polymorph in PVDF by both the above methods. Also, the composite shows a ∼20% larger mechanical property and ∼2 orders higher conductivity than those obtained in the noncovalent functionalized MWNT/PVDF composites with a polythiophene-based compatibilizer,[52] and an attempt has been made to get insight into this important variation in structural, mechanical, and conductivity properties of PVDF upon addition of MWNT-IL.

2. EXPERIMENTAL SECTION

2.1. Materials. PVDF (M_w = 180 000; PDI = 2.57, head to head (H−H) defect = 4.33 mol %) was purchased from Aldrich Chemical Co. USA. The polymer was recrystallized from a 0.3% solution (w/v) in acetophenone, washed with methanol, and dried at 60 °C in vacuum. 1-Methylimidazole, 2-bromoethylamine hydrobromide, and multiwalled carbon nanotubes (MWNTs) (purity 95%, length 0.5−200 μm, and outer diameter 20−30 nm) were purchased from Aldrich Chemical Co. USA and were used as received. Dicyclohexylcarbodiimide (DCC) and *N,N*-(dimethylamino)pyridine (DMAP) (SRL Laboratories, India) were used as received. All the solvents were dried before use.

2.2. Synthesis of MWNT-COOH. Carboxyl-functionalized multiwalled carbon nanotubes (MWNT-COOH) were prepared by oxidation of pristine MWNTs. Into a 250 mL flask equipped with a condenser were added pristine MWNTs (1.0 g), HNO_3 (65%, 10 mL), and H_2SO_4 (98%, 30 mL) with vigorous stirring. The flask was immersed in an ultrasonic bath (40 kHz) for 30 min. The mixture was then stirred for 24 h under refluxed conditions. After cooling the reaction mixture, it was diluted with 250 mL of deionized water and was then filtered under reduced pressure through a polycarbonate membrane (Aldrich, USA) of pore size 0.22 μm. The solid was redispersed in 100 mL of water and was filtered again. The dispersion, filtering, and washing steps were repeated until the pH of the filtrate reached 7. The filtered solid was then dried under vacuum for 12 h at 60 °C to produce 750 mg of carboxylic acid-functionalized MWNTs.

2.3. Synthesis of the Amine-Terminated Ionic Liquid (IL-NH_2). In a two-necked flask, 1-methylimidazole (5.2 g, 0.065 mol) and dry ethanol (35 mL) were added, and the mixture was stirred in a nitrogen atmosphere. 2-Bromoethylamine hydrobromide (13 g, 0.066 mol) was then added to the flask and was refluxed at stirring conditions over 24 h. After that the liquid was separated, and the remaining solid was washed three times with ethanol. Then it was transferred with ethanol, and solvent was evaporated. The resulting compound was washed with dry ethyl acetate several times and was dried at 50 °C to give the product IL-NH_2. ^{1}H NMR (D_2O, 300 MHz): δ = 8.86 (s, 1H), 7.56 (s, 1H), 7.48 (s, 1H), 4.56 (t, 2H), 3.71 (t, 2H), 3.42 ppm (m, 2H). IL-NH_2 is soluble in ethanol, DMF, and DMSO and very soluble in water,

2.4. Synthesis of MWNT-IL by Amidation Reaction. MWNT-IL was prepared by an amidation reaction between MWNT-COOH and IL-NH_2. In a 250 mL flask, a dispersed solution of MWNT-COOH (250 mg), IL-NH_2 (500 mg), dicyclohexylcarbodiimide (DCC, 500 mg), and *N,N*-(dimethylamino)pyridine (DMAP) was taken in DMF (50 mL) and was sonicated for 15 min. Then the mixture was vigorously stirred at 50 °C for 24 h. After the reaction, unreacted MWNTs and IL-NH_2 were removed by centrifugation with ethanol several times. MWNT-IL was subsequently filtered through a 0.22 μm polycarbonate membrane and was thoroughly washed with ethanol and water repeatedly and finally dried in vacuum to get the 3-aminoethyl imidazole functionalized MWNT (MWNT-IL). Yield: 200 mg.

2.5. Preparation of PVDF/MWNT-IL Composite Films. The MWNT-IL was dispersed in *N,N*-dimethyformamide (DMF) by

sonication for 10 min in an ultrasonic bath (60 W, model AV10C, Eyela), and it was stable for months. An amount of 1 g of PVDF was dissolved in DMF to make a 2% (w/v) solution by heating the mixture at 70 °C for 2 h. The PVDF solution was mixed with the MWNT-IL solution in the required proportion to produce different compositions of MWNT-IL in PVDF (0.05, 0.1, 0.2, 0.5, and 1% (w/w)) of the nanocomposites. They were homogenized by sonication for 10 min, and the films were cast by evaporation of the solvent on flat dishes at 70 °C under a pool of air. They were finally dried in vacuum at 70 °C for 3 days to obtain the solvent cast samples. The melt-blended samples were prepared by melting the intimate mixture (prepared at mortar pestle) of the components at required compositions at 220 °C for 20 min to make them homogeneous and then slowly cooled to room temperature. The process was repeated 2−3 times and finally made PVDF/MWNT-IL melt-blending composite samples. The designations of the composite samples are presented in Table 1.

Table 1. Composition and Designation of the PVDF/MWNT-IL Nanocomposite Samples

	sample code	
composition of MWNT-IL (wt %) in PVDF	solvent cast	melt blending
0	PVDF	PVDFM
0.05	PMI0.05	PMI0.05M
0.1	PMI0.1	PMI0.1M
0.2	PMI0.2	PMI0.2M
0.5	PMI0.5	PMI0.5M
1	PMI1	PMI1M

2.6. Characterization. *Spectroscopy.* ^{1}H NMR spectra were measured from a Bruker 300 MHz spectrometer in D_2O. FT-IR spectra of the samples were obtained from thin films cast from their solutions using a Perkin-Elmer FT-IR instrument (spectrum 100). Raman spectra were obtained with a LabRam HR800 high-resolution Raman spectrometer (Horiba-Jobin Yvon) using a 632.8 nm wavelength laser source.

Microscopy. The functionalization of MWNTs with ionic liquid and dispersion of MWNT-IL in the PVDF matrix were studied using a transmission electron microscope (TEM, JEOL 2010EX) operated at an accelerated voltage of 200 kV. A drop of the dilute homogeneous solution on the carbon-coated copper grid was initially dried at room temperature and was finally dried in vacuum at 30 °C for 2 days. The morphology of the samples and that of the facture surface was also observed through a field emission scanning electron microscope (FE-SEM, JEOL GSM-5800) after platinum coating. The texture of the blend sample was studied using a polarized optical microscope (Leitz Biomed) equipped with a digital camera.

XRD Study. The wide-angle X-ray scattering experiments of the samples were carried out in a Bruker AXS diffractomer (model D8 Advance) using a Lynx Eye detector. The instrument was operated at a 40 kV voltage and at a 40 mA current. The samples were scanned in the range 2θ = 5−35° with a step width of 0.02° at the scan rate 0.5 s/step.

Thermal Study. The thermal experiments of the samples were made in a Perkin-Elmer differential scanning calorimeter (Diamond DSC-7) equipped with Pyris software. The samples taken in an aluminum pan (4−5 mg) were heated from −25 to 220 °C at the heating rate 40 °C/min under a nitrogen atmosphere. The higher heating rate was chosen to avoid melt-recrystallization of PVDF.[55a] The sample was then kept at 220 °C for 5 min and was cooled at the cooling rate of 5 °C/min to −25 °C where it was kept for 10 min for attaining equilibrium. Then, the samples were again heated to 220 °C at the heating rate 20 °C/min. The melting (T_m) and crystallization (T_c) temperatures were taken as their respective peak temperatures. The enthalpy values were obtained from the peak area measured using the Pyris software. The thermogravimetric analysis (TGA) experiments were performed using a TA Instrument (model SDT Q 600) under a nitrogen atmosphere at a heating rate of 10 °C/min.

Mechanical Property. The dynamic mechanical properties of the samples were measured using a dynamic mechanical analyzer (DMA) (TA Instruments, model Q-800) at a constant frequency of 1 Hz with a static force of 0.02 N. The films (dimension: 25 × 5 × 0.15 mm) were made from the composites by solution casting on a die, and they were installed on the film tension clamp of the calibrated instrument. The samples were heated from −100 to 150 °C at a heating rate of 10 °C/min. The storage modulus and tan δ values were measured. The melt-blended films of the above dimensions were also used to measure the above properties.

Tensile tests were carried out for the films of uniform thickness using a universal testing machine (Zwick Roell, model Z005) at a strain rate of 1 mm/min at room temperature (30 °C). Each experiment was repeated four times to observe reproducibility. Both solvent-cast and melt-blended films were used in the work.

Conductivity. The dc-conductivity of the film samples was measured by a two-probe technique with an electrometer (Keithley, model 617). The samples were prepared by sandwiching between the two gold electrodes, and conductivity was measured at 30 °C using the equation

$$\sigma = \frac{1}{R} \times \frac{d}{a}$$

Scheme 1. Schematic Illustration for Functionalization of MWNTs by Ionic Liquid (MWNT-IL)

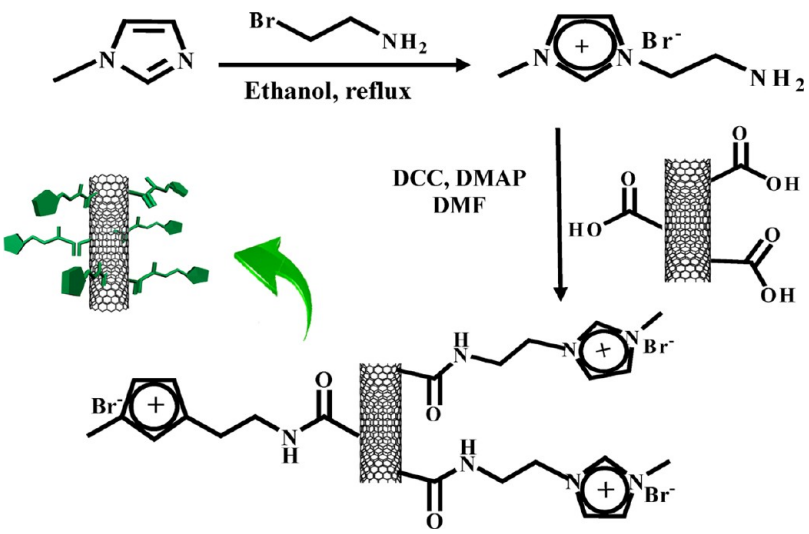

where d is the thickness; a is the area measured by a screw gauge and slide calipers; and R is the resistance of the sample measured from the electrometer.

3. RESULTS AND DISCUSSION

3.1. Functionalization of MWNTs with Ionic Liquid and Characterization. The functionalization of MWNTs with ionic liquid is depicted in Scheme 1. The chemical oxidation of MWNTs was carried out in a HNO_3/H_2SO_4 under sonication conditions to yield carboxylic acid functionalized MWNTs. Amine-terminated IL (IL-NH_2) is prepared by treating 1-methylimidazole with 2-bromoethylamine hydrobromide, and the ionic liquid modified MWNTs (MWNT-IL) are synthesized from an amidation reaction between the MWNT-COOH and the IL-NH_2. The covalent functionalization between MWNT-COOH and IL-NH_2 is demonstrated by FT-IR spectroscopy (Figure 1a). In MWNT-COOH the >C═O bands appeared at 1716 and 1584 cm^{-1}, indicating the presence of carboxylic acid groups, and after amidation reaction, the >C═O band of the carboxylic acid group shifts to 1630 cm^{-1}, indicating the formation of the amide bond between MWNT-COOH and IL-NH_2.[55b]

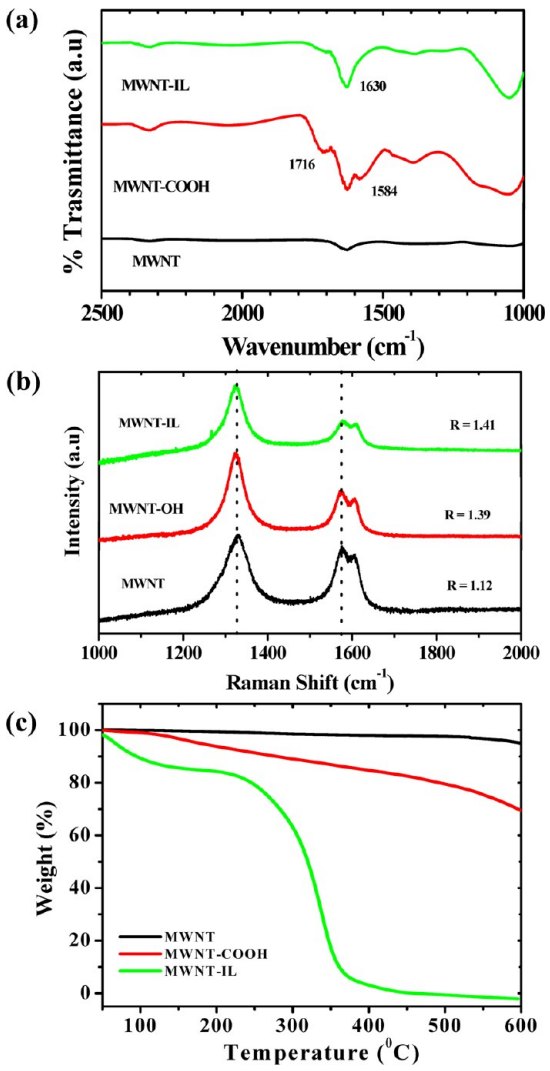

Figure 1. (a) FT-IR spectra of MWNTs, MWNT-COOH, and MWNT-IL. (b) Raman spectra of pristine MWNTs, MWNT-COOH, and MWNT-IL, respectively. (c) TGA curves for pristine MWNTs, MWNT-COOH, and MWNT-IL.

Raman spectroscopy is a powerful instrument to get important information about the covalent modification of the MWNTs.[56,57] In the Raman spectra (Figure 1b) of the pristine MWNTs, the "D" band at 1325 cm^{-1} is assigned to defects in the MWNT lattice with sp^3-hybridized carbon, and the "G" band at 1577 cm^{-1} is for the vibrations of the sp^2-hybridized framework. In covalent functionalization of the MWNTs the sp^2-hybridized carbon transforms into sp^3-hybridized carbon, and the increase of the intensity ratio of the D and G band ($R = I_D/I_G$) is an indication of covalent functionalization. After oxidation of MWNTs, the D and G bands of MWNT-COOH are shifted to 1323 and 1573 cm^{-1}, respectively, and the R value increases from 1.12 for MWNTs to 1.39 for MWNT-COOH, indicating an increase in the number of surface defects.[57] After amidation reaction with IL-NH_2, the resulting MWNT-IL again demonstrates a small increase of the ratio (R = 1.41). The increase of R from 1.39 in MWNT-COOH to R = 1.41 in MWNT-IL might be due to the cation−π interaction between MWNTs and IL, apart from the existing covalent linkages.

The thermal stability of the IL-functionalized MWNTs is determined from the TGA data[58,59](Figure 1c). The pristine MWNTs are thermally stable up to 600 °C; in contrast, the MWNT-IL decomposes at much lower temperature with two main weight-loss regions: (i) at ∼240 °C, attributed to the decomposition of the surface-attached (aminoethyl)-imidazolium salt, and (ii) at ∼350 °C, a significant weight loss is likely to the decomposition of MWNTs. The quantity of the 3-aminoethyl imidazole in MWNT-IL is determined from the TGA diagram by comparing with that of MWNT-COOH,[59] and a 10.8 wt % loss for the aminoethyl imidazole fragments is detected. From this value the mol % of the aminoethyl imidazole moiety on the surface of MWNTs is calculated to be 1.13 mol % (the molecular weight of the aminoimidazole fragment = 114.2 g/mol). During heating of MWNT-IL in the TGA thermograms, the (aminoethyl imidazolium) part becomes detached, probably retaining some carboxy-nitrogenous moiety in the MWNT backbone, and on further increase in temperature, this moiety helps in the degradation of MWNTs. It is to be noted here that MWNT-COOH does not degrade at this temperature to such a large extent. The nature of the carboxy-nitrogenous moiety and the involved reaction mechanism is yet unknown.[55b,59]

The morphology and tubular structure of the functionalized MWNTs were observed in transmission electron micrographs. The TEM images (Figure 2) of pristine MWNTs and MWNT-IL systems indicate that the pristine MWNTs are entangled with each other, but in the later system the MWNTs are well dispersed and are also thicker than the former. The average thickness of pristine MWNTs is (22.5 ± 1.7) nm and of MWNT-IL is (36.8 ± 1.3) nm. From the data, it is evident that the average thickness of the IL present on the MWNT surface is ∼10 nm, which suggests a significant coating of the ionic liquid on the MWNT surface due to the covalent functionalization.

3.2. Characterization of PVDF and MWNT-IL Composites. Physically, both the solvent cast and the melt-blended composite films are flexible, hard, and gray colored, and they are completely different from that of PVDF films which are flexible, soft, and translucent at room temperature.

3.2.1. Morphology. To understand the dispersion of MWNT-IL in the PVDF matrix, the FE-SEM micrographs of

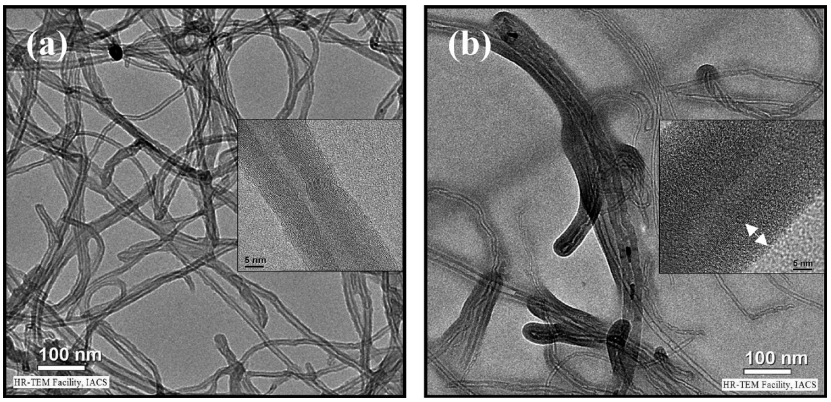

Figure 2. TEM images of (a) pristine MWNTs and (b) IL-functionalized MWNTs (MWNT-IL).

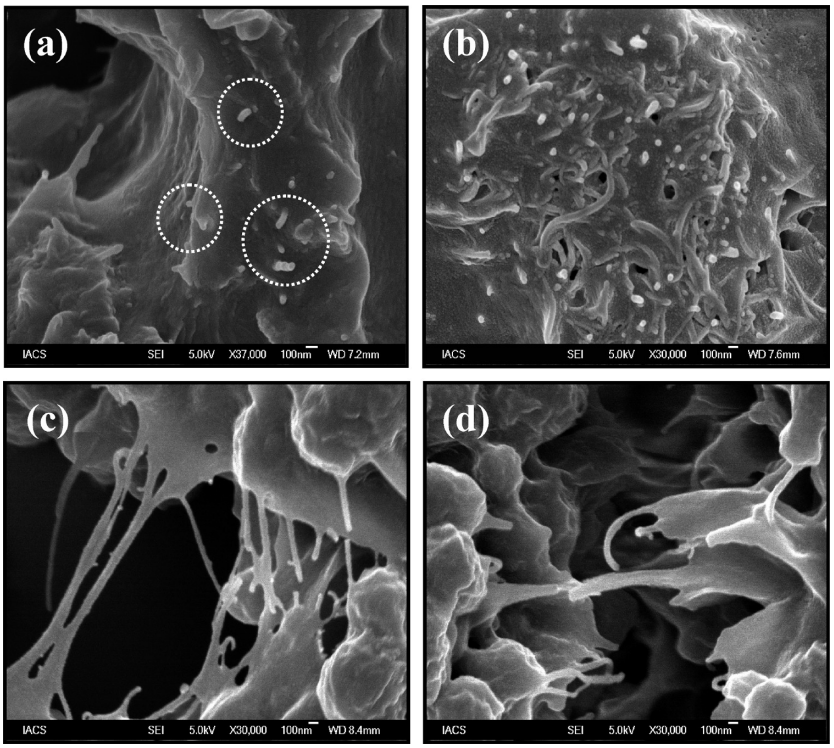

Figure 3. FE-SEM images of PVDF/MWNT-IL nanocomposites. (a) PMI0.5, (b) PMI1, and freeze-fractured surface of (c) PMI0.2 and (d) PMI0.5 samples, respectively.

PVDF/MWNT-IL (PMI) nanocomposite films and their freeze-fractured surfaces are presented in Figure 3(a−d). The MWNT-ILs are found to remain well-dispersed within the PVDF matrix as evident from the white spots (in circular mark, Figure 3a). The IL-modified MWNTs are found to be homogeneously and singly dispersed in the polymer matrix, suggesting a considerable improvement in the compatibility of MWNTs in PVDF. In PMI1 it is evident that there is a good dispersion of MWNTs; however, some MWNT-ILs are also found at the surface which may arise due to the greater population of MWNT-IL compared to PMI0.5. The dispersion of MWNTs can be better visualized from the freeze-fractured cross section (Figure 3(c,d)) of PMI composites.[51,52] The threads of MWNTs are clearly observed in both images suggesting the three-dimensional network structure of MWNTs in the composites, and it indicates that the presence of IL-containing MWNTs improves the homogeneous dispersion in the PVDF matrix. In the corresponding TEM micrographs (Figure 4(a−d)), of PMI composites, it is evident that with increasing MWNT-IL concentration the MWNTs are well dispersed within the PVDF matrix. The density of MWNTs gradually increases with an increase of filler concentration, and it indicates that MWNTs are well dispersed even at 1% (w/w) MWNT-IL concentration. At each image, the polymer layers surrounding the MWNTs are clearly observed.

In Figure 5(a−d), the polarized optical micrographs of PVDF and PVDF/MWNT-IL nanocomposites are presented. PVDF (Figure 5a) exhibits a well-defined spherulitic morphology of the α polymorph.[48,49] In the PMI0.2 sample, the spherulitic morphology has become gradually lost, and in PMI0.5 the birefringence pattern of PVDF is almost absent. This is probably due to the formation of a major fraction of the β phase which does not exhibit any birefringence pattern.[42] However, in the micrograph of PMI1, the four-lobe spherulitic morphology is not observed, suggesting a complete transformation of the β phase (cf. FT-IR and WAXD results).[50,51]

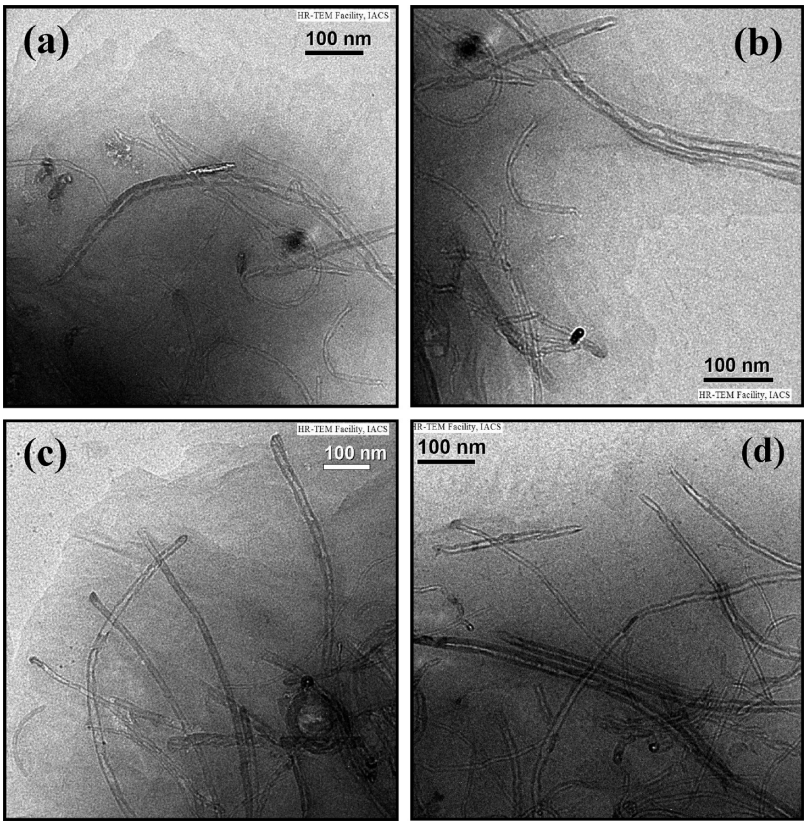

Figure 4. TEM images of PVDF and IL-functionalized MWNT nanocomposites. (a) PMI0.1, (b) PMI0.2, (c) PMI0.5, and (d) PMI1 samples, respectively.

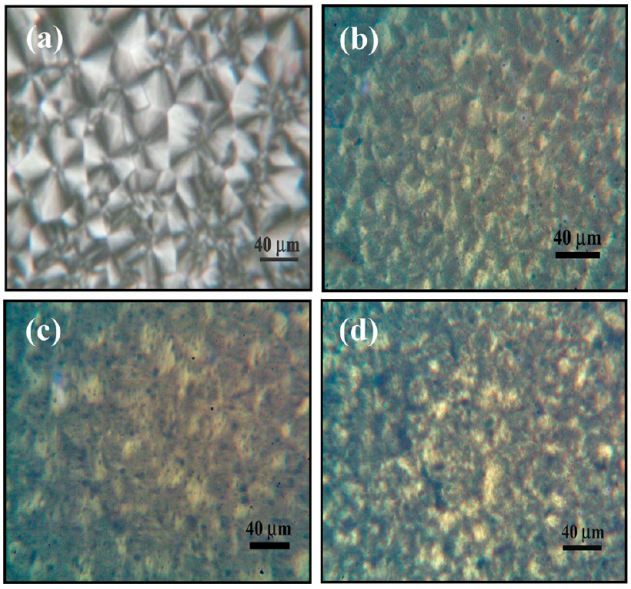

Figure 5. Polarized optical micrographs of (a) PVDF, (b) PMI0.05, (c) PMI0.5, and (d) PMI1 samples produced by isothermal crystallization.

However, in the micrograph some birefringence is observed which might arise from the supramolecular organization of MWNT-IL with PVDF as the former does not exhibit any birefringence (Supporting Information, Figure 1). Hence, in the PMI composites, it may be argued that MWNT-IL may be present within the PVDF matrix as shown in a schematic model (Scheme 2), causing a variation in spherulitic texture.

Scheme 2. Schematic illustration for the dispersion of ionic liquid functionalized MWNTs within the PVDF matrix

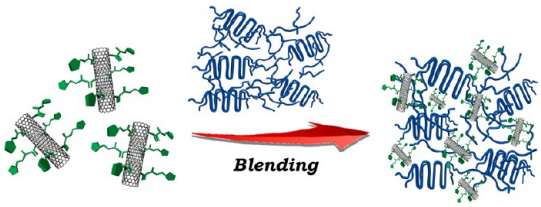

3.2.2. Structure. 3.2.2.1. FT-IR Spectra. FT-IR spectra have been used to determine the structure of PVDF and also to understand the supramolecular interaction between MWNT-IL and PVDF. Figure 6(a,b) presents the FT-IR spectra of neat PVDF, PMI composites of solvent cast, and melt-blended films with different compositions of MWNT-IL. PVDF shows transmittance peaks at 532, 615, 764, 796, and 976 cm^{-1} characterizing the formation of the α-phase at both solvent cast and melt-blending conditions.[48−51,60−64] On addition of MWNT-IL in PVDF, the intensity of the α-peaks gradually decreases, and the intensity of 1275, 840, 510, and 445 peaks gradually increases. The peaks at 445, 510, 840, and 1275 cm^{-1} characterize the formation of the piezoelectric β-phase.[48−51,60−64] With increasing MWNT-IL concentration, the intensity of the later peaks gradually increases, indicating the formation of increased percentage of the β-phase. It is to be noted here that 510 and 840 cm^{-1} peaks also correspond to the γ phase, but the presence of the 1275 cm^{-1} peak confirms that PVDF is crystallizing in the β phase in the composites.[42b] In PMI1 (1 wt % MWNT-IL) the complete transformation of the β-phase occurs in both solution and melt-blending samples.

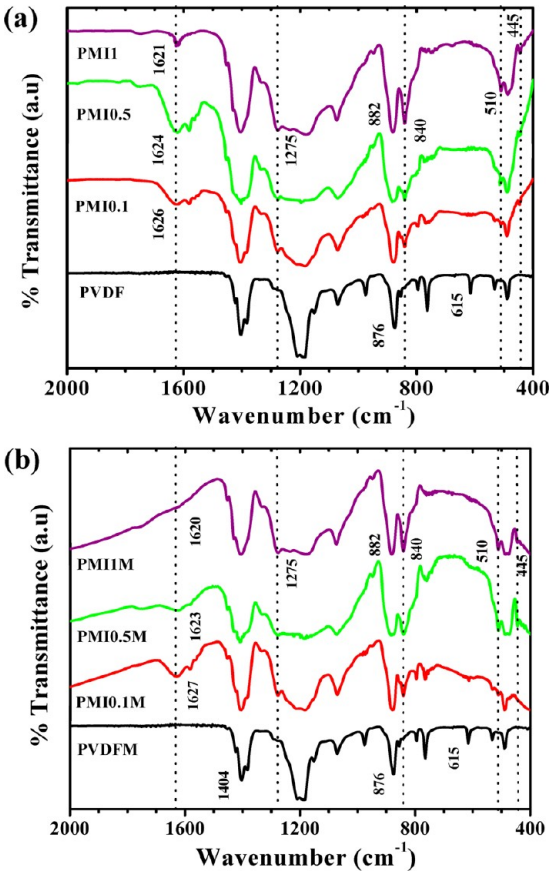

Figure 6. FT-IR spectra of (a) solvent cast and (b) melt-blended samples of PVDF/MWNT-IL composites at the indicated MWNT-IL concentration.

The MWNT-IL has an amide (−CONH−) stretching peak at 1630 cm^{-1} (Figure 1a), and in the composites with PVDF this peak shows a gradual shift to lower energy from 1626 cm^{-1} in PMI0.05 to 1620 cm^{-1} in PMI1. This is due to the dipolar interaction between −CONH− groups of MWNT-IL with the $>CF_2$ dipoles of PVDF. The CF−CH−CF bending vibration of PVDF at 876 cm^{-1} shows a shift to higher energy (879, 882, 883, and 884 cm^{-1}) in the composites with increasing MWNT-IL concentration due to the increased specific interaction.[62−64] Also, it should be mentioned here that some specific interaction between the imidazolium cation with $>CF_2$ dipole may exist[54b] which also contributes to the shift of the CF−CH−CF bending vibration to higher energy. This interaction with the imidazolium cation probably renders the $>CF_2$ dipole to be located along one side of the molecular chain. Therefore, due to the dipole−dipole interaction, the all-trans conformation of PVDF is adopted on the surface of IL-coated MWNTs. The adsorption energy for the β polymorph is higher than that of the α phase, and a large amount of energy is required for transforming "*TGTG*" into "*TTTT*" conformations.[65] So, only a few percent of the β phase was observed when pristine MWNTs were used in the PVDF matrix.[52] However, the interaction between the $>CF_2$ group of PVDF with ionic liquid functionalized MWNTs can overcome such an energy barrier between the α and β phase, and a larger amount of β crystals are produced due to the dispersion of the IL-coated MWNTs in PVDF. Due to this specific interaction between the ionic liquid functionalized MWNTs with PVDF, it also causes a homogeneous dispersion of MWNTs into the PVDF matrix and assists the formation of β crystals at both the fabrication conditions.[50,51]

3.2.2.2. X-ray Diffraction (XRD). The formation of a β polymorph of PVDF in the composites is also evident from the WAXD spectra (Figure 7(a,b)) for the solvent cast and melt-blended samples, respectively. It is apparent that pure PVDF exhibits four characteristic diffraction peaks at 2θ = 17.8, 18.5, 20.0, and 26.7° which are assigned to (100), (020), (110), and (021) reflections of α-phase PVDF crystals.[50−52,66−68] However, in the PMI composites (both solvent cast and melt-blended) the α characteristic diffraction peaks are observed with decreased intensity, and at the PMI1 sample only a single peak at 2θ = 20.3° is observed. This peak corresponds to the (110) and (200) crystal planes of the most important piezoelectric β phase PVDF[66,67] indicating a 100% β-phase formation and stabilization in the PMI1 composite. However, in the other PMI composites, the diffraction peaks of the α crystal become reduced, indicating a mixture of α and β phase formation. This result suggests that at the immediate vicinity of the MWNT surface the nucleation of the β phase crystal occurs, and it grows to form β phase crystals.[52] However, at low MWNT concentration (≤0.5 wt %), the nucleation can not be all β phase for the lack of sufficient MWNTs surface, and some α phase crystals nucleate at the bulk, causing a mixture of α and β phases.[50,52] This means that a critical concentration of MWNT-IL in PVDF is necessary to induce the 100% β-phase of PVDF formation at both the fabrication conditions. We note that the WAXD results are highly consistent with the FT-IR results. A comparison of polymorphic transition from α to β phase using physically functionalized MWNT and covalently functionalized MWNT with ionic liquid in the composites with PVDF may be made here. We have reported a 100% transformation into β phase with PMI1 and PMI1M samples,

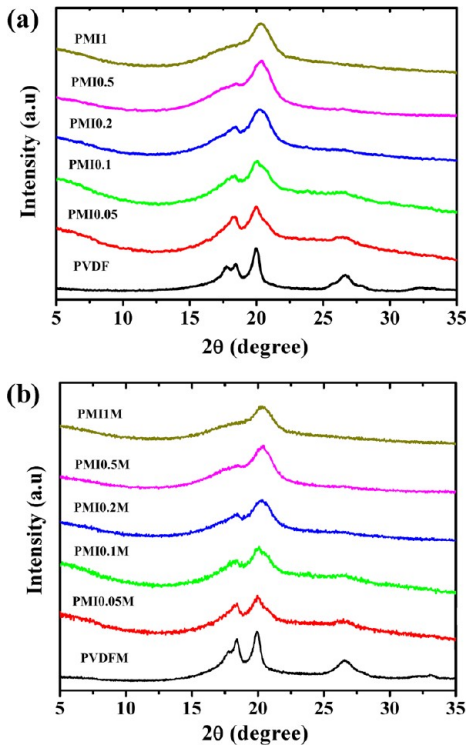

Figure 7. WAXD spectra of (a) solvent cast and (b) melt-blended samples of PMI composites at the indicated MWNT-IL composition.

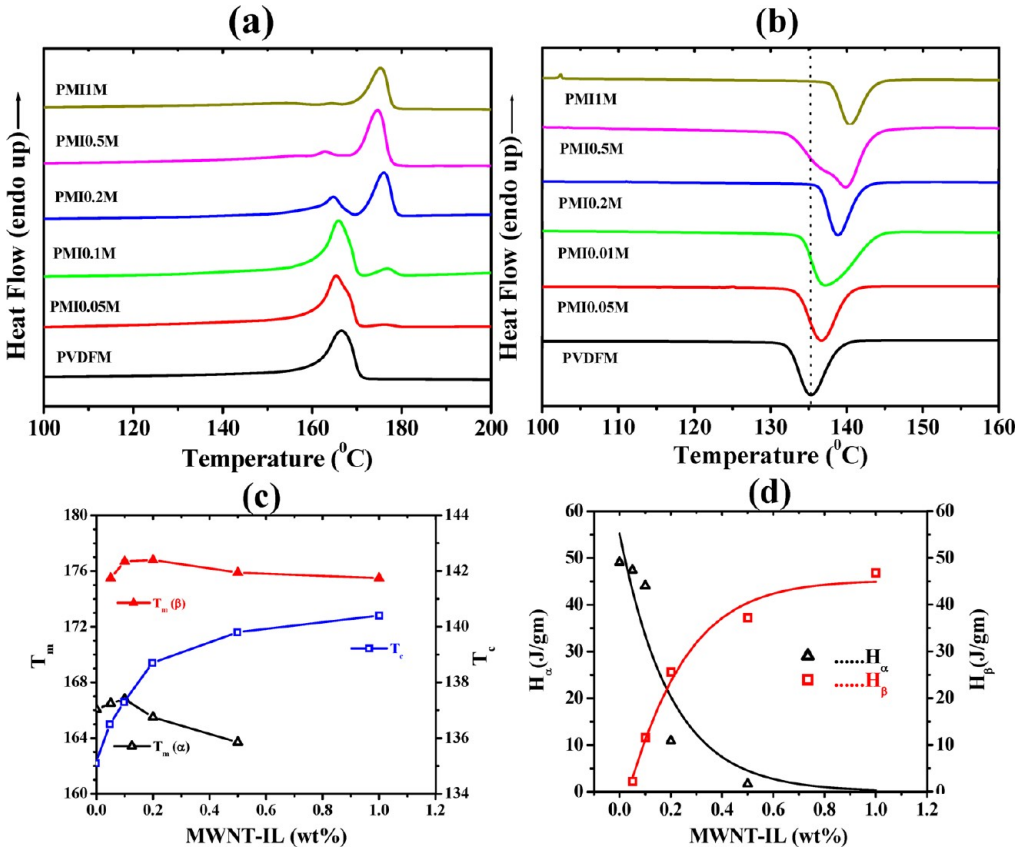

Figure 8. DSC melting (a) and (b) cooling endotherms of PVDF/MWNT-IL nanocomposites at indicated compositions for melt-blended samples. (c) Plot of melting (T_m) and crystallization (T_c) temperature of PMIM composites with an increase of MWNT-IL. (d) Plot of ΔH_α and ΔH_β phases with MWNT-IL content (w/w %) (obtained from heating thermograms of melt-blended samples).

while using a physically functionalized MWNT with ionic liquid[54b] produces a combination of β and γ phases. In the present case, only 1 (w/w)% MWNT-IL is required, but 2 (w/w)% MWNT and 2 (w/w)% IL are required for complete transformation into the polar form of PVDF. So, the covalently linked IL with MWNT is more efficient to induce polar form formation of PVDF than physically modified ILs and MWNTs. A probable explanation is the combined interaction from the anchored −CONH group and imidazolium group of the MWNT-IL with the >CF_2 group of PVDF, whereas in the case of the physically functionalized MWNT, only the interaction from the imidazolium group takes place.

3.2.3. Thermal Properties. Figure 8(a,b) illustrates DSC heating and cooling curves of pure PVDF and its PMI composites for melt-blended samples, and they are illustrated in Supporting Information Figure 2 for the solvent cast samples. It is apparent from Figure 8a that pure PVDF exhibits a single melting temperature (T_m) at about 167 °C, but the solvent cast sample melts at 165 °C with a hump at the higher-temperature region (Supporting Information, Figure 2a)[49,51] that has been attributed to the melt recrystallization of α crystals.[55,69,70] From the figure, it is apparent that on addition of MWNT-IL in PVDF a new peak appears at higher temperature, and the peak size increases on increasing MWNT-IL concentration for both categories (melt-blend and solvent cast) of samples. From the FT-IR and WAXS data, it is evident that PMI0.2, PMI0.5, and PMI1 samples contain β crystals; also, it is known that the melting temperature of the α phase is lower than that of the β phase for PVDF.[42b,70] For the PMI1 sample, only one melting peak at 175 °C is observed, suggesting it to be obviously originated from the melting of the pure β crystals in the nanocomposites. Hence the higher melting peaks in the above thermograms may be attributed to the β phases. In Figure 8c the melting temperatures of α and β phases of PMIM samples are plotted, and a maximum is noted for both the α and β phases. The initial increase of T_m with MWNT concentration is due to the good dispersion of MWNT-ILs in PVDF causing a compact and higher melting crystal due to the surface forces of MWNTs attracting each other.[71] With further increase of MWNTs, a decrease of melting temperature of both phases of the composite occurs, and it may be attributed to the specific interaction between PVDF and MWNT-IL at the melt.[72,73] At this higher filler concentration, the distribution of the filler is such that the interaction of the MWNT surface is isotropic, consequently nullifying the forces causing a lesser compact crystal. It is to be noted that the decrease of melting temperature of the β phase is not as prominent as that in the α phase, and it may be attributed to the formation of a higher amount of β phase crystal which is more compact than α phase. So, here IL acts as a good interfacial adhesive agent between MWNTs and the PVDF matrix, and it plays an important role for the homogeneous dispersion of MWNTs in the PVDF matrix.

The DSC cooling thermograms of the corresponding samples are shown in Figure 8b and Supporting Information Figure 2b when the samples are cooled from 220 °C at the rate of 5 °C/min. The crystallization temperature (T_c) of neat PVDF is located at 134.7 °C, and it progressively shifts to

higher temperature when MWNT-ILs are added into the PVDF matrix. This means that the MWNT-IL acts as a nucleating agent for PVDF and accelerates the crystallization of PVDF.[70] In melt-blended composites the transition of α phase to β phase can be visualized from the enthalpy of fusion value of the corresponding crystal phases (Figure 8d), and the ratio of α and β polymorphs produced in PVDF/MWNT-IL composites can be obtained. It is apparent that the amount of β polymorph increases with a concomitant decrease of the α polymorph with increasing MWNT-IL content in the composite. One development that may be consistent with the data is that the MWNT-IL is nucleating the β crystal on its surface, and the α crystal is nucleating at the bulk. It is shown that the incorporation of IL-modified MWNTs into the PVDF matrix not only accelerates the crystallization of PVDF but also induces the formation of β-form crystals simply crystallized from the melt state. The nucleation synergetic effects by MWNT-ILs can be attributed to the dipolar and specific interaction between the PVDF molecular chains with the imidazium-containing ionic liquid functionalized from the surface of MWNTs.[54,70] Such interaction enhances the formation of the oriented zigzag conformation of PVDF chains and accelerates the crystallization of PVDF.

3.2.4. Dynamic Mechanical Properties. In Figure 9 the storage modulus (G') and tan δ vs temperature plots of the melt-blended composites are presented. It is apparent that with an increase of temperature the G' of PVDF and PMIM samples gradually decreases in a nonlinear way. With an increase of MWNT-IL concentration, the G' values gradually increase, showing a maximum rise for the PMI0.5 M sample. The solvent cast composites also exhibit almost similar behavior in dynamic mechanical properties presented in the Supporting Information, Figures 3 and 4. The G' values of different compositions of both types of composites are presented in Table 2 where the percentage increase of G' values from that of PVDF is also compared. It is apparent from the table that in the composites there is a substantial increase of G' values at all the temperatures for both categories of the samples, and it is attributed to the reinforcing effect of MWNTs due to its high aspect ratio and its homogeneous dispersion. The maximum increase of G' values is found in the viscoelastic region for all the composites (0−50 °C), and the maximum increase (101.3%) is observed at the PMI0.5 M sample. A probable reason is that at this composition the MWNT-ILs are better dispersed than that of the other melt-blended samples. In the solvent cast samples the maximum increase of G' values is 98.3% for the PMI0.5 sample at 50 °C. Those MWNT-ILs which are effectively dispersed in the bulk can cause better enhancement in mechanical properties than those dispersed in the surface. In PMI1 some MWNT-ILs are found at the surface, but it is absent in the PMI0.5 samples (Figure 3b). Hence, PMI0.5 exhibits the highest increase in mechanical property compared to that of PMI1. It is necessary to mention here that the highest increase of G' values in PVDF composites with other covalently functionalized MWNTs is 66−67%,[9,50,51] but in this case the maximum increase is 101.3%, a considerably higher value. A probable reason may be the stronger interfacial interaction contributed from both the −CONH group and imidazolium cation attached to MWNT-IL with the $>CF_2$ dipole of PVDF facilitating easier energy transfer, showing a very high reinforcement.

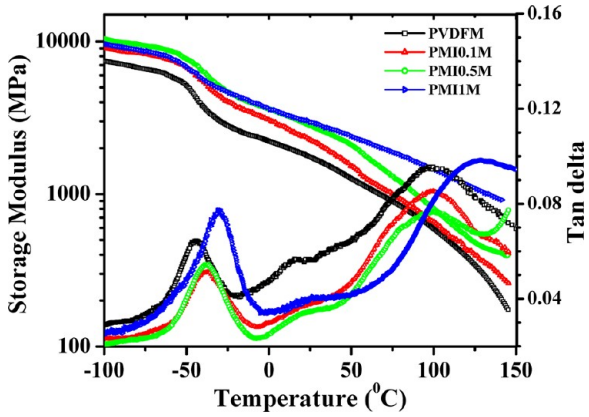

Figure 9. Dynamic mechanical property vs temperature plots of PVDF and the PVDF/MWNT-IL melt-blended nanocomposite films. (a) Storage modulus and (b) Tan delta.

The tan δ vs temperature plot of PVDF shows three peaks at −42.5, 8.2, and 97.7 °C corresponding to the glass transition (T_g) of the PVDF amorphous zone, transition temperatures at the crystal−amorphous interface (T_r(I)), and that within the crystalline zone (T_r(II)), respectively (Table 2).[29,52−54] The melt-blended samples also exhibit similar three transition temperatures; however, the values are higher than that of solvent cast samples, and it may be due to a higher free volume of the solvent cast samples compared to the melt-processed composites. The increase of T_g value with an increase of MWNT-IL concentration in both types of the composites may be attributed to the increased compactness of the amorphous zone of PVDF due to the strong surface force between the MWNTs.[74] The interfacial zone of PVDF also experiences a difficulty in the relaxation process due to the surface forces of the MWNT-IL. The increase of T_r(II) temperature of the composites compared to that of PVDF may be attributed to the same reason as in the amorphous and interfacial zone. The transition temperature of the solvent cast samples behaves almost similarly with the melt-blended composites due to the same surface force of MWNT-IL dispersed in the PVDF matrix. We note that relaxation at the crystalline region (T_r(I) and T_r(II)) requires a larger rise of temperature than that of the amorphous phase in the composites; e.g, for PMI1 the difference in T_g from that of PVDF is 9 °C, while those of T_r(I) and T_r(II) are 17 and 14 °C, respectively. In the case of PMI1M, the difference in T_g from that of PVDF is 12 °C, whereas those from T_r(I) and T_r(II) are 14 and 29 °C, respectively. This increase of difference in transition temperatures for relaxation in the crystalline interface (T_r(I)) and crystalline region (T_r(II)) might be attributed to the change of polymorphic structure from the α to β phase of PVDF. The β phase is more compact (density = 1.99 g/cm^3) than that of the α phase (density = 1.92 g/cm^3) and amorphous phase (1.78 g/cm^3),[37] so it requires higher thermal energy (i.e., higher temperature) for the relaxation. As the transformation into the β phase is complete at PMI1 and PMI1M, a maximum rise of relaxation temperature occurs at this composition. Also the rise in transition temperatures of PMI1 from that of PVDF is higher for the melt-processed sample than solvent cast sample, and it may be due to higher free volume in the solvent cast samples compared to the melt-blended samples.

3.2.5. Mechanical Properties. In Figure 10(a,b), the stress−strain curves of the solvent cast and melt-blended composites are presented. From the curves, it is evident that on increase of

Table 2. Summary of Glass Transition (T_g), Transition Temperatures (T_r), and Storage Modulus (G') Values of PVDF and Their Nanocomposites with MWNT-IL at Different Temperatures

samples	glass transition temperature (T_g)	transition temperature (T_r) T_r(I)	T_r(II)	G' (MPa) at −50 °C	% increase	G' (MPa) at 0 °C	% increase	G' (MPa) at 50 °C	% increase
PVDF	−42.5	8.2	97.7	4947	_	1974	_	1321	_
PMI0.05	−42.2	12.7	100.5	5404	9.2	2798	41.7	1675	26.8
PMI0.1	−41.7	15.2	105.2	6220	25.7	3162	60.2	1847	39.8
PMI0.2	−38.4	16.5	99.0	6726	35.9	3485	76.5	2292	73.5
PMI0.5	−37.8	20.1	99.7	6972	40.9	3743	89.6	2619	98.3
PMI1	−33.8	25.9	111	6765	36.7	3652	85.1	2407	82.2
PVDFM	−43.4	13.5	97.2	5137	-	2225	-	1265	-
PMI0.05M	−39.2	12.8	100.2	6148	19.6	2898	30.2	1601	26.6
PMI0.1M	−38.8	20.5	99.6	6770	31.8	3078	38.3	1532	21.1
PMI0.2M	−42.1	25.6	102.1	7102	38.2	3787	70.2	2093	65.4
PMI0.5M	−36.5	24.1	101.5	7682	49.5	3615	62.5	2547	101.3
PMI1M	−31.2	27.4	126.2	6890	34.1	3612	62.3	2401	89.8

MWNT-IL concentration the tensile strength increases in both categories of the composites, but the elongation at break varies differently. In the solvent cast sample it increases, while in the melt-blend samples it decreases with an increase of MWNT-IL concentration. The Young's modulus, tensile strength, elongation at break, and toughness of solvent cast and melt-blended samples are obtained from the stress−strain plots and are presented in the bar diagrams (Figure 10(c−f)) with different MWNT-IL concentration. It is apparent from Figure 10c that the Young's modulus of the composites increases with increase of MWNT-IL concentration, and melt-blended composites have a higher value than that of solvent cast samples; i.e., for unit strain the stress required is higher in the melt-blended samples than the solvent cast samples. One probable reason is the more compact nature of melt-blended samples. The tensile strength of solvent cast films is also lower over melt-blended samples probably due to the same reason, i.e., lower compactness. The elongation at break of the two types of samples exhibits a drastic difference; in solvent cast samples there is an increase followed by decreases showing a maximum, whereas in melt-blended samples it decreases continuously with increasing MWNT-IL concentration. No definite reason can be afforded here, and it might be due to the better network structure of solvent cast samples which gradually unfold on applying stress[49,52,53] than the melt-blended samples where it decreases due to the increase of stiffness (i.e., modulus) value. From Figure 10f, it is interesting to note that the toughness of the melt-blended samples increases gradually with MWNT-IL concentration, but for the solvent cast samples at lower filler concentration it increases, reaching a maximum at 0.5% MWNT-IL concentration, and then decreases. At all composites of melt-blended samples the toughness values are higher than those of solvent cast samples, and the increase of toughness may be related to the easier transfer of the applied stress through the increased MWNT−PVDF interfaces in the composites.

To understand the orientation of MWNT-IL, the Young's modulus data of both categories of composites are plotted with composition, and they are compared with the theoretical curves drawn using the Halpin−Tsai equation.[75] The modified Halpin−Tsai equation relating the Young's modulus (E_c) of the composites for the random orientation of MWNTs (E_{NT}) with that polymer (E_p) is given as[75,76]

$$E_c^{\,r} = E_p\left[\frac{3}{8}\frac{1 + 2(l_{NT}/D_{NT})\eta_L V_{NT}}{1 - \eta_L V_{NT}} + \frac{5}{8}\frac{1 + 2\eta_T V_{NT}}{1 - \eta_T V_{NT}}\right] \quad (1)$$

and for the unidirectional (i.e., parallel) orientation of the MWNTs to the surface of the composites films

$$E_c^{\,p} = \left[\frac{1 + 2(l_{NT}/D_{NT})\eta_L V_{NT}}{1 - \eta_L V_{NT}}\right] \quad (2)$$

where

$$\eta_L = \frac{(E_{NT}/E_P) - 1}{(E_{NT}/E_P) + 2(l_{NT}/D_{NT})}$$

$$\eta_T = \frac{(E_{NT}/E_P) - 1}{(E_{NT}/E_P) + 2}$$

where $E_c^{\,p}$ is the Young's modulus of the composites where MWNTs are oriented parallel to the surface of the sample films. l_{NT} and D_{NT} refer to the length and diameter of the MWNTs, and V_{NT} is the volume fraction of MWNTs in the nanocomposites. The $E_c^{\,r}$ and $E_c^{\,p}$ values are calculated taking E_p of PVDF = 1.25 GPa, E_{NT} = 1280 GPa, l_{NT} = 12 μm, D_{NT} = 10 nm, density of MWNTs = 2.1 g/mL, and density of PVDF = 1.92 g/mL[18,22,52,76] and are plotted with different volume fractions of MWNTs (Figure 11). From the figure it is apparent that the measured data at low MWNT-IL concentration are closer to the unidirectional orientation, but with the increase of MWNT-IL concentration they follow mostly to the random orientation. This suggests that at lower concentration the MWNTs are first oriented parallel to the surface of the composite films, and above 0.1 (vol % of MWNTs) they adopt almost a random orientation. The lower experimental value at higher MWNT concentration than that of random (theoretical) orientation might be related to the agglomeration of MWNTs with the increasing concentration in both solvent cast and melt-blended composites.

3.2.6. dc-Coductivity. The dc-conductivities of solvent cast and melt-blended samples are measured at 30 °C as a function of MWNT-IL loading and are presented in Figure 12a. PVDF is an insulator having conductivity of 5.46×10^{-13} S/cm. From the figure it is evident that there is a steep increase of

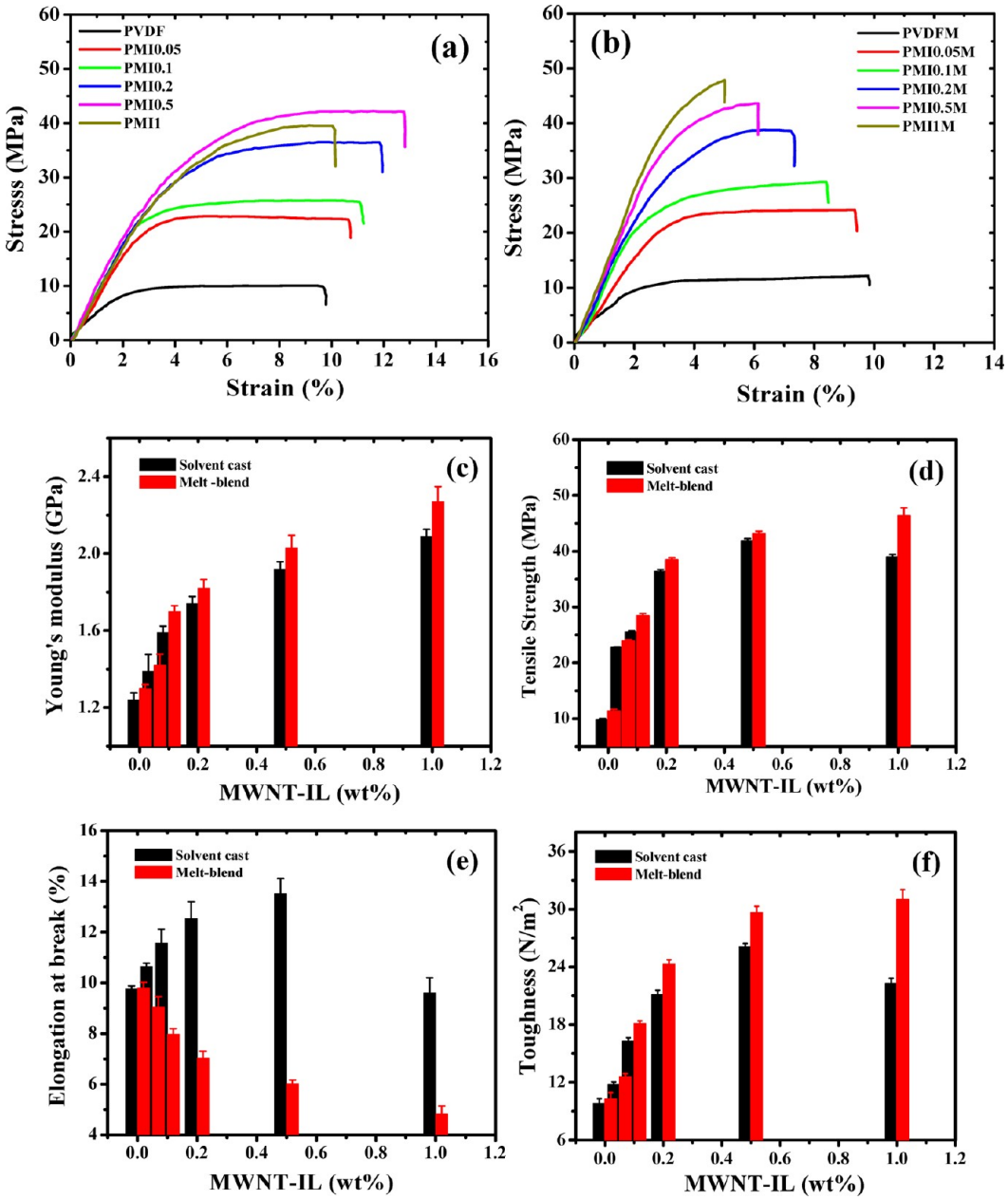

Figure 10. Mechanical properties of PVDF/MWNT-IL composites: representative stress−strain curves of (a) solvent cast and (b) melt-blended samples. The bar diagrams of (c) tensile modulus, (d) tensile strength, (e) elongation at break, and (f) toughness.

conductivity of the composites at low concentration of MWNT-IL, and then it almost levels up, showing the highest conductivity 0.417 and 0.887 S/cm for the PMI1 and PMI1M samples, respectively. The interesting point of these composites is the value of the percolation threshold, i.e., the critical concentration of MWNTs where it generates the conductive pathway throughout the whole sample for the charge transport. The percolation threshold depends on the aspect ratio, the extent of nanofillers dispersion or aggregation, and their self-assembly. Here the system shows a very low percolation threshold at 0.05 wt % (for $\sigma = 10^{-7}$ S/cm) because at this concentration the conductivity exhibits a sharp increase of ∼6 orders of magnitude. The very low percolation threshold compared to HO-MWNT/PVDF (0.25% w/w), unfunctionalized MWNT/PVDF (0.49% w/w), and noncovalent functionalized using polythiophene based compatibilizer (0.06% w/w)[52] is interesting, indicating the existence of a conducting path via highly dispersed MWNT-IL for easy charge transfer. The high aspect ratio of MWNTs and the homogeneous distribution of MWNT-IL in the PVDF matrix allow achieving the very low percolation threshold. The insulator−conductor transition on varying the conductive filler concentration can be depicted from the percolation theory[29,52,77−80]

$$\sigma = \sigma_0(p - p_c)^t \quad \text{when} \quad p > p_c$$

where σ = composite conductivity; σ_0 is a constant; p is the weight fraction; p_c is the percolation threshold; and t is the critical exponent. The conductivity data of the samples are fitted to the above scaling law, and the linear fit to the logarithmic plot of conductivity vs $\log(p - p_c)$ provides the straight line in both solvent cast and melt-blended samples (Figure 12b). From the slope of the straight line, the critical

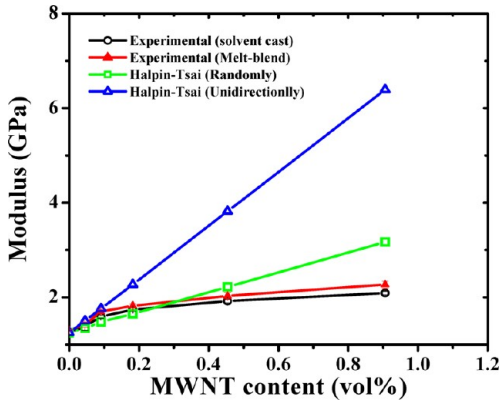

Figure 11. Young's modulus vs loading of MWNTs (vol %) of the PMI composite samples. The Halpin−Tsai equation is used to obtain theoretical data for the random and parallel orientation of MWNTs.

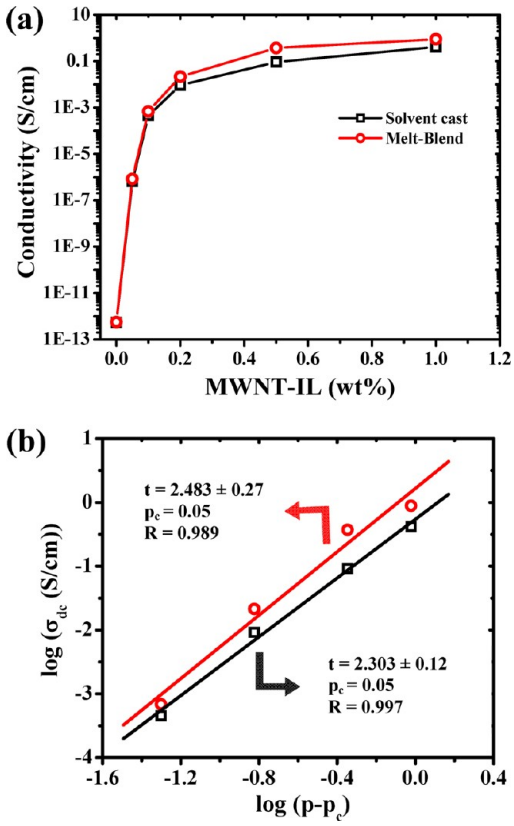

Figure 12. (a) dc-Conductivity of PVDF/MWNT-IL solvent cast and melt-blended composite films as a function of the weight percentage of the MWNT-IL at 30 °C. (b) Linear dependence of $\log(\sigma_{dc})$ with $\log(p - p_c)$ according to the percolation scaling law where the solid line corresponds to the best fitted line for both the samples.

exponent t values are 2.303 ± 0.12 and 2.483 ± 0.27 for the solvent cast and melt-blended samples with their intercept values $(\sigma_0) = 4.47 \times 10^{-2}$ and 4.87×10^{-2} S/cm, respectively. Hence the critical exponent (t) value of the PVDF/MWNT-IL composites is close to the universal value of the three-dimensional percolation network (3-D) ($t = 1.94$),[52,77] and the high conductivity is due to this network formation of MWNTs within the PVDF matrix. The systems obey the three-dimensional percolation mechanism of charge transport between MWNT-ILs in the PVDF matrix. The dc-conductivity of pure MWNT-ILs is calculated using $P = 100$ and $p_c = 0.05$ in the equation, and the values are 44.8 and 56.2 S/cm, for solvent cast and melt-cooled samples, respectively.[78] These values are about one order higher than that of noncovalent functionalized MWNTs with a polythiophene-based compatibilizer[52] or PMMA functionalized MWNTs[29] and two orders lower than that of pure MWNTs.[52,79] Thus a larger improvement in the conductivity of the composites compared to the above covalent and noncovalent functionalized MWNTs is observed. A probable explanation of the higher conductivity may lie in the contribution from the anchored ionic liquid to the MWNTs by delocalization of the charges of the former through the π-clouds of the MWNT surface. Hence, though it is a covalent functionalization (where usually defects become introduced along with shortening of MWNT length), the PVDF/MWNT-IL composite exhibits a very high dc-conductivity.

4.. CONCLUSIONS

Multiwalled carbon nanotubes are functionalized by covalent functionalization with ionic liquid (IL, 3-aminoethyl imidazolium bromide) which helps its good dispersion in the PVDF matrix. The TEM micrographs indicate that the average coating thickness of MWNTs by IL is about 10 nm, and the covalent linkage of IL with MWNT is confirmed from FT-IR and Raman spectra. We have successfully fabricated PVDF nanocomposites with full β-polymorphic form using MWNT-IL as the filler by both solvent cast and melt-blending methods. The FE-SEM and TEM micrographs indicate that IL-bound MWNTs are homogeneously dispersed in the PVDF matrix. The covalently anchored IL not only helps to disperse the MWNTs in the PVDF matrix but also causes the PVDF chains to adopt the all-trans conformations that lead to the formation of piezoelectric β-PVDF crystals. Increasing MWNT-IL concentration in the composites results in the increased amount of β polymorph with a concomitant decrease of α polymorph showing a complete β polymorph formation for 1 wt % MWNT-IL in both the fabrication conditions, and it is the first report to get 100% β PVDF using MWNT filler. A DSC study also shows that the MWNT-ILs are a more efficient nucleating agent for PVDF crystallization, preferentially nucleating the β form due to the dipolar interactions of PVDF with the MWNT-IL. The glass transition temperature (T_g), transition temperatures at the crystal−amorphous interface (T_r(I)), and that within the crystalline zone (T_r(II)) of PVDF gradually increase with an increase in MWNT-IL concentration. The reinforcing effect of MWNT-ILs is significant, showing a maximum increase of G' (101.3%) for the PMI0.5 M sample due to its high aspect ratio and its homogeneous dispersion. The Young's modulus of the composites increases with an increase of MWNT-IL concentration, and analysis of the data using the Halpin−Tsai equation suggests that at low MWNT-IL concentration they adopt parallel orientation to the film surface; however, at higher MWNT-IL concentration, it follows mostly the random orientation. The tensile strength also increases with an increase in MWNT-IL concentration, and both Young's modulus and tensile strength of solvent cast films are lower over melt-blended samples. The elongation at break in the solvent cast samples shows an increase showing a maximum and then decreases, whereas in melt-blended samples it decreases continuously with increasing MWNT-IL concentration. The toughness of the melt-blended samples increases gradually with MWNT-IL concentration, but for the solvent cast samples at lower filler concentration it increases, reaching maximum at

0.5% MWNT-IL concentration, and then decreases. Toughness values are higher for melt-blended samples than those of solvent cast samples. The system shows a very low percolation threshold at 0.05 wt % (for $\sigma = 10^{-7}$ S/cm), and analysis of the conductivity data with percolation theory suggests a three-dimensional conducting network is produced throughout the whole sample. A larger improvement (~2 orders) in the conductivity of the composites compared to the other reported covalent and noncovalent functionalized MWNTs is observed, and a probable explanation of the higher conductivity may lie in the contribution from the anchored ionic liquid to the MWNTs by delocalization of the charges of the former through the π-clouds of the MWNT surface. The complete transformation into the piezoelectric β-polymorph, good mechanical property, and highly improved electrical conductivity suggest the supremacy of MWNT-IL to make multifunctional PVDF nanocomposites.

■ ASSOCIATED CONTENT

Ⓢ Supporting Information

Optical micrograph, DSC scans of solvent cast samples, and dynamic mechanical property data. This material is available free of charge via the Internet at http://pubs.acs.org.

■ AUTHOR INFORMATION

Corresponding Author

*E-mail: psuakn@iacs.res.in. Fax: +91 33 2473 2805.

Notes

The authors declare no competing financial interest.

■ ACKNOWLEDGMENTS

We gratefully acknowledge DST New Delhi (grant no. SR/S1/PC/26/2009) and 'Unit of Nanoscience at IACS' for financial support. A.M. acknowledges CSIR, New Delhi, for the fellowship.

■ REFERENCES

(1) (a) Lubin, G., Ed. In *Handbook of Composites*; Van Nostrand Reinhold: New York, 1982; p 234. (b) Vaia, R. A.; Krishnamoorti, R. In *Polymer nanocomposites: Synthesis, Characterization, and Modeling*; Krishnamoorti, R., Vaia, R. A., Eds.; American Chemical Society: Washington, DC, 2001; p 1.
(2) (a) Ajayan, P. M. *Chem. Rev.* **1999**, *99*, 1787. (b) Ajayan, P. M.; Tour, J. M. *Nature* **2007**, *447*, 1066.
(3) Tasis, D.; Tagmatarchis, N.; Bianco, A.; Prato, M. *Chem. Rev.* **2006**, *106*, 1105.
(4) Niyogi, S.; Hamon, M. A.; Hu, H.; Zhao, B.; Bhowmik, P.; Sen, R.; Itkis, M. E.; Haddon, R. C. *Acc. Chem. Res.* **2002**, *35*, 1105.
(5) Dresselhaus, M. S.; Dresselhaus, G.; Avouris, P. *Carbon Nanotubes: Synthesis Structure, Properties, and Applications*; Springer: Heidelberg, 2001.
(6) Postma, H. W. C.; Teepen, T.; Yao, Z.; Grifoni, M.; Dekker, C. *Science* **2001**, *293*, 76.
(7) Pop, E.; Mann, D.; Wang, Q.; Goodson, K.; Dai, H. *Nano Lett.* **2006**, *6*, 96.
(8) Berber, S.; Kwon, Y. K.; Tomanek, D. *Phys. Rev. Lett.* **2000**, *84*, 4613.
(9) Coleman, J. N.; Khan, U.; Gun'ko, Y. K. *Adv. Mater.* **2006**, *18*, 689.
(10) Moniruzzaman, M.; Winey, K. I. *Macromolecules* **2006**, *39*, 5194.
(11) Kwon, J.; Kim, H. *J. Polym. Sci., Part A* **2005**, *43*, 3973.
(12) Yu, A.; Hui, H.; Bekyarova, E.; Itkis, M. E.; Gao, J.; Zhao, B.; Haddon, R. C. *Compos. Sci. Technol.* **2006**, *66*, 1190.
(13) Li, N.; Huang, Y.; Du, F.; He, X.; Lin, X.; Gao, H.; Ma, Y.; Li, F.; Chen, Y.; Eklund, P. C. *Nano Lett.* **2006**, *6*, 1141.
(14) Yang, Y.; Gupta, M. C.; Dudley, K. L.; Lawrence, R. W. *Nano Lett.* **2005**, *5*, 2131.
(15) Coleman, J. N.; Cadek, M.; Blake, R.; Nicolosi, V.; Ryan, K. P.; Belton, C.; Fonseca, A.; Nagy, J. B.; Gun'ko, Y. K.; Blau, W. J. *Adv. Funct. Mater.* **2004**, *14*, 791.
(16) (a) Lin, Y.; Taylor, S.; Li, H.; Fernando, S.; Qu, L.; Wang, W.; Gu, L.; Zhou, B.; Sun, Y. P. *J. Mater. Chem.* **2004**, *14*, 527. (b) Tran, M. Q.; Cabral, J. T.; Shaffer, M. S. P.; Bismarck, A. *Nano Lett.* **2008**, *8*, 2744.
(17) Jeon, J. H.; Lim, J. H.; Kim, K. M. *Polymer* **2009**, *50*, 4488.
(18) Moore, V. C.; Strano, M. S.; Haroz, E. H.; Hauge, R. H.; Smalley, R. E.; Schmidt, J.; Talmon, Y. *Nano Lett.* **2003**, *3*, 1379.
(19) Chatterjee, T.; Yurekli, K.; Hadjiev, V. G.; Krishnamoorti, R. *Adv. Funct. Mater.* **2005**, *15*, 1832.
(20) Grunlan, J. C.; Liu, L.; Kim, Y. S. *Nano Lett.* **2006**, *6*, 911.
(21) Zou, J.; Khondaker, S. I.; Huo, Q.; Zhai, L. *Adv. Funct. Mater.* **2009**, *19*, 479.
(22) Li, Y.; Shimizu, H. *Macromolecules* **2008**, *41*, 5339.
(23) Chen, J.; Hamon, M. A.; Hu, H.; Chen, Y.; Rao, A. M.; Eklund, P. C.; Haddon, R. C. *Science* **1998**, *282*, 95.
(24) (a) Hirsch, A. *Angew Chem., Int. Ed.* **2002**, *41*, 1853. (b) Baskaran, D.; Mays, J. W.; Bratcher, M. S. *Angew. Chem., Int. Ed.* **2004**, *43*, 2138.
(25) Georgakilas, V.; Kordatos, K.; Prato, M.; Guldi, D. M.; Holzinger, M.; Hirsch, A. *J. Am. Chem. Soc.* **2002**, *124*, 760.
(26) Chen, J.; Ramasubramaniam, R.; Xue, C.; Liu, H. *Adv. Funct. Mater.* **2006**, *16*, 114.
(27) Park, H.; Zhao, J.; Lu, J. P. *Nano Lett.* **2006**, *6*, 916.
(28) Bahr, J. L.; Tour, J. M. *Chem. Mater.* **2001**, *13*, 3823.
(29) Mandal, A.; Nandi, A. K. *J. Mater. Chem.* **2011**, *21*, 15752.
(30) Liu, L.; Grunlan, J. C. *Adv. Funct. Mater.* **2007**, *17*, 2343.
(31) (a) Bergman, J. G.; McFee, J. H.; Crane, G. R. *Appl. Phys. Lett.* **1971**, *18*, 203. (b) Li, Y.; Huang, X.; Hu, Z.; Jiang, P.; Li, S.; Tanaka, T. *ACS Appl. Mater. Interfaces* **2011**, *3*, 4396.
(32) (a) Betz, R. *Ferroelectrics* **1987**, *75*, 397. (b) Chang, C. -M.; Liu, Y. -L. *ACS Appl. Mater. Interfaces* **2011**, *3*, 2204.
(33) (a) Nalwa, H. S., Ed. *Ferroelectric Polymers*; Marcel Dekker: New York, 1995. (b) Nalwa, H. S., Ed. *Handbook of Low and High Dielectric Constant Materials and Their Applications*; Academic Press: London, 1999.
(34) (a) Guiot, J.; Ameduri, B.; Boutevin, B. *Macromolecules* **2002**, *35*, 8694. (b) Zhao, Z.; Zheng, W.; Yu, W.; Long, B. *Carbon* **2009**, *47*, 2112.
(35) Ameduri, B. *Chem. Rev.* **2009**, *109*, 6632.
(36) Baise, A. I.; Lee, H.; Oh, B.; Salomon, R. E.; Labes, M. M. *Appl. Phys. Lett.* **1975**, *26*, 428.
(37) (a) Lovinger, A. J. In *Developments in crystalline polymers-1*; Bassett, D. C., Ed.; Applied Science Publishers: London, 1981; p 195. (b) Lovinger, A. J. *Science* **1983**, *220*, 1115.
(38) Doll, W. W.; Lando, J. B. *J. Macromol. Sci., Phys. B.* **1970**, *4*, 309.
(39) Hasegawa, R.; Takahashi, Y.; Chatani, Y.; Tadokaro, H. *Polym. J.* **1972**, *3*, 600.
(40) Davis, G. T.; Mckinney, J. E.; Broadhurst, M. G.; Roth, S. C. *J. Appl. Phys.* **1978**, *49*, 4998.
(41) Dillon, D. R.; Tenneti, K. K.; Li, C. Y.; Ko, F. K.; Sics, I.; Hsiao, B. S. *Polymer* **2006**, *47*, 1678.
(42) (a) Naegele, D.; Yoon, D. Y.; Broadhurst, M. G. *Macromolecules* **1978**, *11*, 1297. (b) Manna, S.; Nandi, A. K. *J. Phys. Chem. B* **2011**, *115*, 12325.
(43) (a) Hattori, T.; Kanaoka, M.; Ohigashi, H. *J. Appl. Phys.* **1996**, *79*, 2016. (b) Branciforti, M. C.; Sencadas, V.; Lanceros-mendez, S.; Gregorio, R. *J. Polm. Sci., Part B: Polym. Phys.* **2007**, *45*, 2793.
(44) Das-Gupta, D. K.; Doughty, K. *J. Appl. Phys.* **1978**, *49*, 4601.
(45) Lando, J. B.; Doll, W. W. *J. Macromol. Sci., Phys.* **1968**, *B2*, 205.
(46) Wang, J.; Li, H.; Liu, J.; Duan, Y.; Jiang, S.; Yan, S. *J. Am. Chem. Soc.* **2003**, *125*, 1496.
(47) Yee, W. A.; Kotaki, M.; Liu, Y.; Lu, X. H. *Polymer* **2007**, *48*, 512.

(48) (a) Priya, L.; Jog, J. P. *J. Polym. Sci., Part B: Polym. Phys.* **2002**, *40*, 1682. (b) Priya, L.; Jog, J. P. *J. Polym. Sci., Part B: Polym. Phys.* **2003**, *41*, 31.
(49) Shah, D.; Maiti, P.; Gunn, E.; Schmidt, D. F.; Jiang, D. D.; Batt, C. A.; Giannelis, E. P. *Adv. Mater.* **2004**, *16*, 1173.
(50) Manna, S.; Batabyal, S. K.; Nandi, A. K. *J. Phys. Chem. B* **2006**, *110*, 12318.
(51) (a) Manna, S.; Nandi, A. K. *J. Phys. Chem. C* **2007**, *111*, 14670. (b) Levi, N.; Czerw, R.; Xing, S. Y.; Iyer, P.; Carroll, D. L. *Nano Lett.* **2004**, *4*, 1267.
(52) Mandal, A.; Nandi, A. K. *J. Phys. Chem. C* **2012**, *116*, 9360.
(53) Layek, R. K.; Samanta, S.; Chatterjee, D. P.; Nandi, A. K. *Polymer* **2010**, *51*, 5846.
(54) (a) Shang, S. M.; Zeng, W.; Tao, X. M. *J. Mater. Chem.* **2011**, *21*, 7274. (b) Xing, C.; Zhao, L.; You, J.; Dong, W.; Cao, X.; Li, Y. *J. Phys. Chem. B* **2012**, *116*, 8312.
(55) (a) Nandi, A. K.; Mandelkern, L. *J. Polym. Sci., Part B: Polym. Phys.* **1991**, *29*, 1287. (b) Park, M. J.; Lee, J. K.; Lee, B. S.; Lee, Y.-W.; Choi, I. S.; Lee, S. -G. *Chem. Mater.* **2006**, *18*, 1546.
(56) Zhang, Y.; He, H.; Gao, C.; Wu, J. *Langmuir* **2009**, *25*, 5814.
(57) Sahoo, N. G.; Cheng, H. K. F.; Li, L.; Chan, S. H.; Judeh, Z.; Zhao, J. *Adv. Funct. Mater.* **2009**, *19*, 3962.
(58) Baskaran, D.; Mays, J. W.; Bratcher, M. S. *Angew. Chem., Int. Ed.* **2004**, *43*, 2138.
(59) Kong., H.; Gao, C.; Yan, D. Y. *J. Mater. Chem.* **2004**, *14*, 1401.
(60) Gregorio, R. *J. Appl. Polym. Sci.* **2006**, *100*, 3272.
(61) Yee, W. A.; Kotaki, M.; Liu, Y.; Lu, X. H. *Polymer* **2007**, *48*, 512.
(62) Roerdink, E.; Challa, G. *Polymer* **1980**, *21*, 509.
(63) Belke, R. E.; Cabasso, I. *Polymer* **1988**, *29*, 1831.
(64) (a) Tashiro, K.; Kobayashi, M.; Tadokoro, H. *Macromolecules* **1981**, *14*, 1757. (b) Tashiro, K.; Kobayashi, M. *Phase Trans.* **1989**, *18*, 213.
(65) Yu, S. S.; Zheng, W. T.; Yu, W. X.; Zhang, Y. J.; Jiang, Q.; Zhao, Z. *Macromolecules* **2009**, *42*, 8870.
(66) Hasegawa, R.; Takahashi, Y.; Chatani, Y.; Todokoro, H. *Polym. J.* **1972**, *3*, 600.
(67) (a) Datta, J.; Nandi, A. K. *Polymer* **1997**, *38*, 2719. (b) Maiti, P.; Nandi, A. K. *Polymer* **1998**, *38*, 2171.
(68) Guerra, G.; Karasz, F. E.; MacKnight, W. J. *Macromolecules* **1986**, *19*, 1935.
(69) Prest, W. M.; Luca, D. J. *J. Appl. Phys.* **1975**, *46*, 4138.
(70) Andrew, J. S.; Clarke, D. R. *Langmuir* **2008**, *24*, 670.
(71) Kuila, B.; Malik, S.; Batabyal, S. K.; Nandi, A. K. *Macromolecules* **2007**, *40*, 278.
(72) Nishi, T.; Wang, T. T. *Macromolecules* **1975**, *8*, 909.
(73) Maiti, P.; Nandi, A. K. *Macromolecules* **1995**, *28*, 8511.
(74) Liu, Z.; Marechal, P.; Jerome, R. *Polymer* **1997**, *38*, 4925.
(75) Halpin, J. C.; Kardos, J. L. *Polym. Eng. Sci.* **1976**, *16*, 344.
(76) (a) Qian, D.; Dickey, E. C.; Andrews, R.; Rantell, T. *Appl. Phys. Lett.* **2000**, *76*, 2868. (b) Cadek, M.; Coleman, J. N.; Barron, V.; Hedicke, K.; Blau, W. J. *Appl. Phys. Lett.* **2002**, *81*, 5123. (c) Yuan, W.; Li, W.; Mu, Y.; Park, M. B. C. *ACS Appl. Mater. Interface* **2011**, *3*, 1702.
(77) Stauffer, G. In *Introduction to Percolation Theory*; Taylor & Francis: London, 1985.
(78) Barrau, S.; Demont, P.; Peigney, A.; Laurent, C.; Lacabanne, C. *Macromolecules* **2003**, *36*, 5187.
(79) Kim, Y. J.; Shin, T. S.; Choi, H. D.; Kwon, J. H.; Chung, Y. C.; Yoon, H. G. *Carbon* **2005**, *43*, 23.
(80) Bello, A.; Laredo, E.; Marval, J. R.; Grimau, M.; Arnal, M. L.; Muller, A. J.; Ruelle, B.; Dubois, P. *Macromolecules* **2011**, *44*, 2819.